

Blur Removal via Blurred-Noisy Image Pair

Chunzhi Gu, Xuequan Lu, *Member, IEEE*, Ying He, *Member, IEEE*, and Chao Zhang, *Member, IEEE*

Abstract—Complex blur such as the mixup of space-variant and space-invariant blur, which is hard to model mathematically, widely exists in real images. In this paper, we propose a novel image deblurring method that does not need to estimate blur kernels. We utilize a pair of images that can be easily acquired in low-light situations: (1) a blurred image taken with low shutter speed and low ISO noise; and (2) a noisy image captured with high shutter speed and high ISO noise. Slicing the blurred image into patches, we extend the Gaussian mixture model (GMM) to model the underlying intensity distribution of each patch using the corresponding patches in the noisy image. We compute patch correspondences by analyzing the optical flow between the two images. The Expectation Maximization (EM) algorithm is utilized to estimate the parameters of GMM. To preserve sharp features, we add an additional bilateral term to the objective function in the M-step. We eventually add a detail layer to the deblurred image for refinement. Extensive experiments on both synthetic and real-world data demonstrate that our method outperforms state-of-the-art techniques, in terms of robustness, visual quality, and quantitative metrics.

Index Terms—Image deblurring, optical flow, Gaussian mixture model

I. INTRODUCTION

IT is prevalent to adopt image deblurring techniques to recover quality images from blurry images. A common situation is capturing photos in dimly-lit environments (e.g., photographing moving objects in a night scene), where one can hardly get sharp and bright photos. Most likely, the taken photos are dark or blurry, depending on the camera settings and object conditions. Though a lower shutter speed can effectively increase brightness, it almost inevitably leads to blur. On the other hand, increasing the shutter speed makes the camera sensor or film exposed to limited light, resulting in dark photos. Setting a high ISO for increasing brightness is a trade-off way to obtain bright photos. Nevertheless, a higher gain setting amplifies noise which may even worsen the photo quality. Recovering quality photos from such captured blurry photos remains challenging and can hardly be resolved by the existing image deblurring techniques.

Removing blur from blurred images to achieve latent sharp images has been widely studied [36], [51]. Many approaches [13], [26] estimate the blur kernels using salient features. Such methods may fail when images are not bright enough to get sufficient features such as edges. In fact, it is difficult to model blur in real photos in some cases, because of the mix of different types of blur (i.e., complex blur). As a result,

C. Gu and C. Zhang* are with the School of Engineering, University of Fukui, Fukui, Japan (e-mails: gu-cz@monju.fuis.u-fukui.ac.jp; zhang@u-fukui.ac.jp).

X. Lu is with School of Information Technology, Deakin University, Geelong, VIC 3216, Australia (e-mail: xuequan.lu@deakin.edu.au).

Y. He is with School of Computer Science and Engineering, Nanyang Technological University, Singapore (e-mail: YHe@ntu.edu.sg).

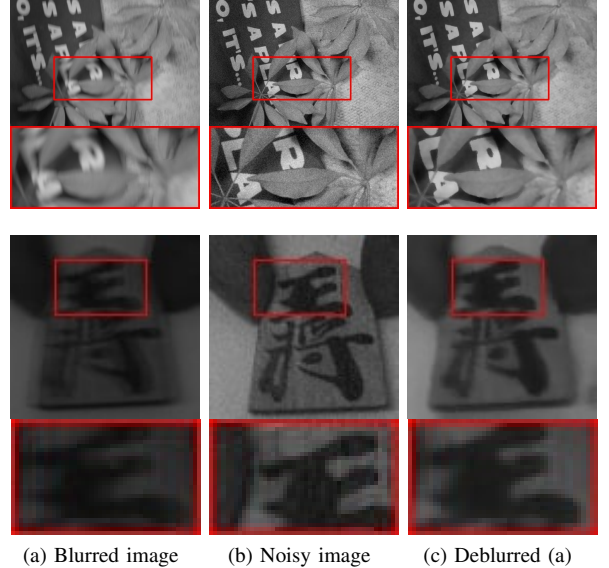


Fig. 1: Deblurring synthetic (row 1) and real-world (row 2) images. Note that (b) is in a different view from (a) and (c). In the synthetic example: (a) is blurred by a mixup of two types of blur and (b) contains synthetic Gaussian noise ($\sigma = 10$). In the real-world example: (a) is taken with the shutter speed of 1 second and ISO of 100 (both the camera and the object are moving); (b) is taken with the shutter speed of 1/20 second and ISO of 1600, and further enhanced.

deblurring methods based on blur kernel estimation have limited performance in handling complex blur.

Compared with a single image, multiple images often show more information that can be utilized for deblurring. In this work, we attempt to exploit a pair of blurred/noisy images which can be easily obtained by changing the shutter speed and ISO settings. The noisy image contains complementary pixel information to the blurred image. Deblurring using a pair of blurred/noisy images has been sparsely treated so far [2], [58], and a close work to ours is Yuan *et al.* [58] in which the noisy image is used to add details lost in the deblurring process with deconvolution. Despite its convincing deblurring performance, it still suffers from two major issues: (1) the image pair is strictly constrained to be taken from the same view, which is to avoid the misalignment of pixels between two images; and (2) the blur kernel in their paper is supposed to be a single type (linear motion blur) caused by camera shake. These two constraints diminish its practical use, for example, the moving objects in row 2 of Fig. 1. As such, their technique has limited performance in the cases without meeting the above assumptions.

To overcome the above limitations, we propose a novel

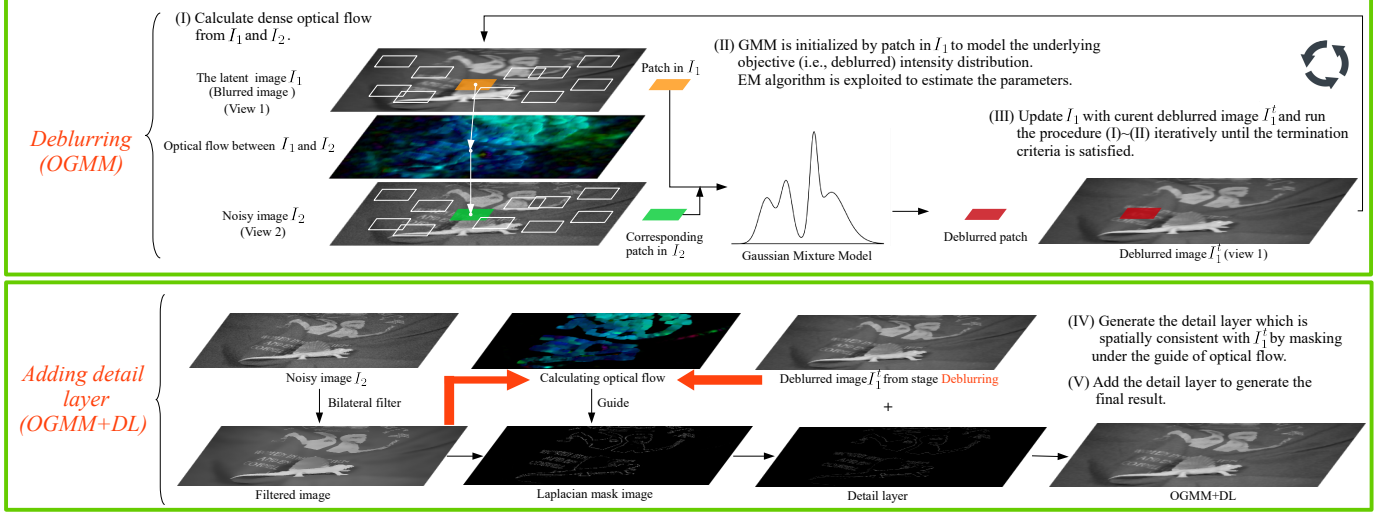


Fig. 2: Overview of our image deblurring approach. The *Deblurring* stage is an iterative procedure. The deblurred image I_1^{t+1} at the $(t+1)$ -th iteration is updated based on the deblurred result I_1^t at the t -th iteration. In the *Adding Detail Layer* stage, the detail layer can be extracted using the Laplacian mask image. The spatial inconsistency between I_1^t and the detail layer is solved by the updated optical flow.

approach for image deblurring, with the easily obtained noisy/blurred image pair. Specifically, we first slice the blurred image (in view 1) into patches and each patch is guided to its corresponding patch in the noisy image (in view 2) by optical flow. To remove the blur and recover the latent sharp image, we extend the Gaussian Mixture Model (GMM) to model the intensity distribution of the latent sharp image, with its parameters estimated by the Expectation-Maximization (EM) algorithm. We further add a bilateral term to the objective function in the M-step of EM, to better preserve sharp features in images. We alternately update the optical flow and perform the EM algorithm for several rounds, to achieve desired deblurring results. Therefore, we refer to our method as optical flow guided GMM (OGMM). To further retain details, we add a detail layer (the denoised sharp features) back to the deblurred image, according to the pixel correspondences from the final estimated optical flow. Our method is free of blur kernels, and it can handle complex blur which is challenging for kernel estimation based techniques (e.g., space-variant blur in the first row of Fig. 1).

The main contributions of this paper are threefold. First, we propose a novel deblurring approach called optical flow guided GMM (OGMM) with a pair of blurred/noisy images as input. Second, we formulate deblurring as a parameter estimation problem, and derive an EM algorithm to optimize the involved parameters. Eventually, a bilateral term is added to the objective function of the M-step in EM to better preserve sharp features, and a detail layer is extracted to enhance the details in the deblurred image. Instead of kernel estimation or deconvolution, we make full use of the noisy image taken in a different view for deblurring.

II. RELATED WORK

Blind deblurring for single image. Blind deblurring aims to accurately estimate the unknown blur kernel, based on

which deconvolution is performed to recover the corresponding sharp image. There are several types of methods for blind deblurring, such as maximum a posterior (MAP) [28], [54], variational Bayes [20], [52], [66], edge prediction [23], [26] and sparse coding [60], [65]. For the MAP based methods, various strategies are presented to cope with the problem revealed by Levin *et al.* [30] that the failure of naïve MAP may occur because it favors no-blur explanations. Marginal distributions are considered to be maximized over all possible images [20], [30]. Image regularizations are introduced into the MAP framework [28], [42], [55] to retain salient image structures. The state-of-the-art methods for single image deblurring also depend on rich information hidden in the blur. Bai *et al.* [3] used reweighted graph total variation as prior to reconstruct a skeleton patch from the blurry observation. Kheradmand *et al.* [27] introduced a novel data adaptive objective function to handle challenging motion blur PSFs. Zhang *et al.* [65] established an unified framework for natural image restoration using group-based sparse representation. Yan *et al.* [57] proposed an image prior named Extreme Channels Prior (ECP) to help the uniform kernel estimation based on the observation that the values of bright channel pixels are likely to decrease. Hu *et al.* [25] utilized light streaks in the images taken in low light situations as constraints for estimating the blur model, but it only succeeds when the light streak is large. Single image blind deblurring usually encounters the bottleneck that the useful information for kernel estimation is insufficient, and can hardly output a proper blur model in real cases. Recently, deep learning based deblurring methods have also been explored [29], [38], [56]. Xu *et al.* [56] emphasized the use of CNN on motion kernel estimation, which performs well mostly on linear motion kernels. To further free the algorithm from the restrictions of blur kernel estimation, Nah *et al.* [38] and Kupyn *et al.* [29] proposed the networks that can handle complex blur

kernels.

Multiple images deblurring. Efforts have been made to multiple images deblurring [9], [11], [22], [31], [43], [58], [64], [67]. The superiority of deblurring with multiple images lies in the complementary information provided in those images. Hee *et al.* [22] introduced a Gyro-Based method to cope with handshake blur caused by camera motion. Multiple blurred images can provide necessary frequency components which are missing due to blur. However, it can hardly handle object movement. Cai *et al.* [9] aligned multiple motion blurred frames accurately and show promising results with their tight framelet system. Li *et al.* [31] used two well-aligned blurred images to better estimate the blur kernel. Zhang *et al.* [64] estimate the latent sharp image with given multiple blurry and/or noisy images by designing a penalty function which can balance the effects of observations with varying quality and avoid local minimal. However, they assume a single type of linear motion blur or uniform blur. *In fact, none of the above approaches can handle complex blur.* To pursue better solutions in solving non-uniform blur, other methods [2], [12], [15], [16], [63], [68] have been proposed, in which they leveraged different forms of multiple observations, e.g., a blurred-noisy pair [2], a blurred-flash pair [68] and multiple blurred images [12], [15], [16], [63]. Arun *et al.* [2] exploited the gradient information on the noisy image to iteratively estimate the latent sharp image, and they seemed to show the results on the data with less intense blurs, according to the provided visual experiments. Cho *et al.* [12] proposed a registration based deblurring strategy, with the constraint that the dominant blur directions of the two input blurred images are required to be approximately orthogonal. In essence, [12], [15], [16], [63], [68] can hardly handle the blur arising from object movement, which are less powerful than our method.

Patch based GMM framework. Gaussian mixture model has been widely exploited in image restoration tasks [44], [46], [47], [53], [62], [69], [18], [59], [61] and point cloud processing tasks [32]–[34]. In [69], Gaussian mixture priors are learned from a set of natural images. By maximizing the expected patch log likelihood, an image without distortion can be reconstructed with priors. The learned patch group Gaussian mixture model (PG-GMM) by Xu *et al.* [53], providing dictionaries and regularization parameters, achieves a high denoising performance. The study by Zoran *et al.* [70] gives a comprehensive analysis that modeling natural images by GMM is effective in log likelihood scores, denoising performance and sample quality. However, GMM based learning methods commonly suffer from huge computational time and a massive dataset. We exploit GMM in a different way, which relates the patches in the noisy image with the patches in the latent image of the blurred image according to dense optical flow. In other words, we attempt to model the intensity distribution in each patch instead of learning patch based image priors to restore images.

III. METHOD

Fig. 2 illustrates the overview of our method, which consists of two stages: deblurring and adding detail layer. The latter

can be viewed as post-processing or refinement. We first adopt optical flow [19] to find the corresponding patches between the blurred image and the noisy image. We then formulate the image deblurring problem under the framework of GMM, and adopt the EM algorithm [17] to optimize the involved parameters. We further add a bilateral term to the objective function in the M-step, to prevent sharp features being smoothed out. Optical flow update and the EM algorithm are alternately called, to achieve the best deblurring results. Finally, we extract a detail layer from the noisy image and add it to the deblurred image, to better preserve the details.

A. Patch Correspondence

The blurred image I_1 is decomposed into a set of overlapping square patches $C = \{c_1, \dots, c_i, \dots, c_P\}$, where $c_i \in R^M$ and $M = s_1 \times s_1$. P is the number of the patches, and s_1 denotes the patch size in I_1 , and M is the number of pixels in each patch. The multiset of pixel intensities in an arbitrary patch from I_1 is denoted as X ($X \in R^M$), and x_m denotes the m -th pixel intensity in X . We adopt the dense optical flow (DOF) [19] to find c_i 's corresponding patch d_j in the noisy image I_2 . Note that for brighter and clearer visualization purposes, in the case of real images, brightness and contrast of I_2 are obtained by adjusting gain, bias, and gamma correction parameters. Here, patch c_i has correspondence to patch d_j if the two center pixels of c_i and d_j are connected with respect to the DOF field. The set of corresponding patches in I_2 can then be denoted as $D = \{d_1, \dots, d_j, \dots, d_P\}$, where $d_j \in R^K$, $K = s_2 \times s_2$. s_2 is the patch size in I_2 . We empirically set $s_2 > s_1$ to ensure sufficient training data for GMM. The pixel intensity multiset of an arbitrary d_j is indicated as Y , $Y \in R^K$, and y_k is the k -th pixel intensity in Y .

B. The Probabilistic Model

Our key idea is to model the underlying distribution of pixel intensities X with the noisy observation Y . We use $X = \{x_m\}$ to denote the corresponding latent pixel intensities, for slight notation misuse. We directly model the pixel intensities instead of the whole patch because the latter will suffer from significantly larger computation burden and noticeable interference due to increased size. To relate X with Y , we assume that y_k follows a GMM whose centroids are $\{x_m\}$. That is, the GMM with those centroids can generate the noisy observations. Thus, we formulate the deblurring problem under the GMM probabilistic framework. Inspired by Myronenko *et al.* [37], we define the probability density function of y_k as

$$p(y_k) = (1 - \omega) \sum_{m=1}^M \frac{1}{M} p(y_k|x_m) + \omega \frac{1}{K}, \quad (1)$$

where $p(y_k|x_m) = \frac{1}{(2\pi\sigma_m^2)^{\frac{d}{2}}} e^{-\frac{\|y_k-x_m\|^2}{2\sigma_m^2}}$ denotes the m -th Gaussian component, and d is the dimension of x_m and y_k ($d = 1$ for gray image). An additional uniform distribution $\frac{1}{K}$ accounts for the noise, with a weight ω . $\sigma^2 = \{\sigma_1^2, \dots, \sigma_m^2, \dots, \sigma_M^2\}$ stands for the covariances and $\frac{1}{M}$ represents the equal membership probability for all the Gaussian components. The centroids of

the GMM model are initialized by X . We next need to find the centroids and covariances that can best explain the distribution of Y .

C. EM optimization

The centroids and covariances of the GMM can be estimated by minimizing the *negative* log-likelihood function [6].

$$E(X, \boldsymbol{\sigma}^2) = - \sum_{k=1}^K \log \left(\frac{1-\omega}{M} \sum_{m=1}^M p(y_k|x_m) + \omega \frac{1}{K} \right). \quad (2)$$

We use the expectation-maximization (EM) algorithm [17] to solve Eq. (2). The EM algorithm consists of two steps: E-step and M-step. E-step and M-step are alternately called for multiple iterations to achieve decent estimations.

E-step. The posterior probability $p^{old}(x_m|y_k)$ is calculated based on Bayes' theorem and the parameters in the previous iteration. p_{mk}^{old} represents $p^{old}(x_m|y_k)$ for simplicity.

$$p_{mk}^{old} = \frac{e^{-\frac{\|y_k-x_m\|^2}{2\sigma_m^2}}}{\sum_{m=1}^M e^{-\frac{\|y_k-x_m\|^2}{2\sigma_m^2}} + \frac{\omega M (2\pi\sigma_m^2)^{\frac{d}{2}}}{(1-\omega)K}}. \quad (3)$$

M-step. The M-step is to update the involved parameters (X and $\boldsymbol{\sigma}^2$) based on the computed posteriors. This is equivalent to minimizing the upper bound of Eq. (2). “new” means calculating the posterior probability with the parameters to be estimated in the current iteration.

$$\begin{aligned} Q(X, \boldsymbol{\sigma}^2) &= - \sum_{k=1}^K \sum_{m=1}^M p_{mk}^{old} \log \frac{\left(\frac{1-\omega}{M} p^{new}(y_k|x_m) + \frac{\omega}{MK}\right)}{\left(\frac{1-\omega}{M} p^{old}(y_k|x_m) + \frac{\omega}{MK}\right) p_{mk}^{old}} \\ &\propto \sum_{k=1}^K \sum_{m=1}^M p_{mk}^{old} \frac{\|y_k-x_m\|^2}{2\sigma_m^2} + \sum_{k=1}^K \sum_{m=1}^M \frac{p_{mk}^{old}}{2} \log \sigma_m^2. \end{aligned} \quad (4)$$

D. Bilateral Term

Eq. (4) can be treated as a data term, which in this work is to numerically approximate Y with X . However, this data term only takes the pixel intensity distribution into account, without considering the spatial information. As illustrated in Fig. 3(a), sharp edges would become coarse (e.g., discontinuity) in the iteration of EM. To overcome this problem, we propose to add a bilateral term to the objective function in M-step. Inspired by the bilateral filter [48], we define the bilateral term B as

$$B(X) = \sum_{m' \in N(m)} \|x_m - x_{m'}\|^2 e^{-\frac{d_{m'}^2}{2\sigma_d^2} - \frac{l_{m'}^2}{2\sigma_l^2}}, \quad (5)$$

where $m' \in N(m)$ denotes a neighbour pixel with its intensity equals to $x_{m'}$. $d_{m'}$ and $l_{m'}$ are the spatial distance and the difference of intensity value between the neighbour pixel m' and the center pixel m , respectively. σ_d and σ_l are constants to control the degree of smoothness.

Redefining Eq. (4) as $D(X, \boldsymbol{\sigma}^2)$ and weighing it with λ , the final objective function can be written as

$$Q(X, \boldsymbol{\sigma}^2) = \lambda D(X, \boldsymbol{\sigma}^2) + (1-\lambda) B(X). \quad (6)$$

We next need to minimize Eq. (6), to solve the involved parameters.

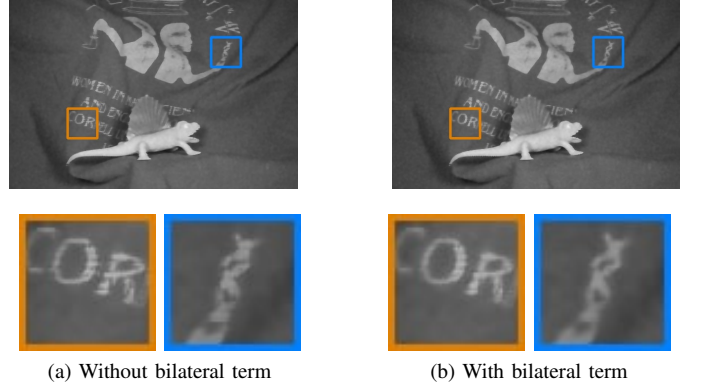


Fig. 3: Deblurred results with and without the bilateral term: (a) without the bilateral term (i.e., $\lambda = 1.0$ in Eq. (6)); (b) with the bilateral term ($\lambda = 0.75$ in Eq. (6)).

E. Minimization

In this section we explain how to solve the optimum solutions of x_m and σ_m^2 . We first take the partial derivation of Eq. (6) with respect to x_m ,

$$\frac{\partial Q(X, \boldsymbol{\sigma}^2)}{\partial x_m} = \frac{\lambda}{\sigma_m^2} \sum_{k=1}^K p_{mk}^{old} (x_m - y_k) + (1-\lambda) \sum_{m' \in N(m)} \frac{2(x_m - x_{m'})}{e^{\frac{d_{m'}^2}{2\sigma_d^2} + \frac{l_{m'}^2}{2\sigma_l^2}}}. \quad (7)$$

Given the mathematical difficulty to directly equate Eq. (7) to zero and solve x_m , due to the x_m in $l_{m'}^2$, we apply gradient descent to approximate the optimum x_m instead. Gradient descent shares the huge advantage in its efficiency to iteratively update the value of x_m with the manual step value. In each gradient descent step x_m is updated as

$$x_m^{q+1} = x_m^q + \alpha \left(\lambda \frac{\sum_{k=1}^K p_{mk}^{old} (y_k - x_m^q)}{\sum_{k=1}^K p_{mk}^{old}} - \mu \sum_{m' \in N(m)} \frac{x_m^q - x_{m'}^q}{e^{\frac{d_{m'}^2}{2\sigma_d^2} + \frac{l_{m'}^2}{2\sigma_l^2}}} \right), \quad (8)$$

where $\mu = 2 \frac{\sigma_m^2 (1-\lambda)}{\sum_{k=1}^K p_{mk}^{old}}$, $q+1$ and q denote the $(q+1)$ -th and q -th gradient descent iteration respectively. α represents the gradient descent step, which is set to 0.1 in our experiments. Eq. (8) is obtained by empirically scaling the gradient of Eq. (7) by $\sigma_m^2 / \sum_{k=1}^K p_{mk}^{old}$ for the convenience of better controlling the gradient descent. μ plays a role in adjusting the proportion of the bilateral term. In general, we take $\mu \in [0.1, 1.0]$ as a controllable parameter for simplicity. Notice that p_{mk}^{old} is not updated in the gradient descent iteration for lowering computational burden.

x_m is updated to x_m' after the gradient descent meets the termination criterion (in the experiment, the iteration stops if the iteration number reaches 50). We take the partial derivative of Eq. (6) with respect to σ_m^2 . By solving $\partial Q / \partial \sigma_m^2 = 0$, σ_m^2 is

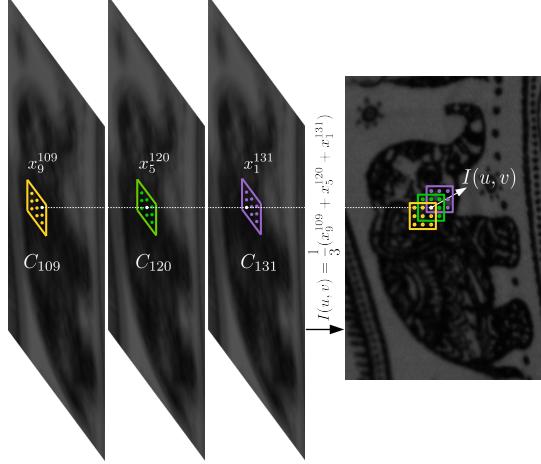


Fig. 4: Illustration of how the pixel value x_m of an arbitrary pixel m located at (u, v) is calculated from multiple overlapped patches. Here, three overlapping patches c_i , (here $i = 109, 120, 131$) are assumed, which contain pixel intensity valued x_9 , x_5 and x_1 , respectively. The final pixel intensity x_m located at (u, v) is calculated as the average of x_9^{109} , x_5^{120} , and x_1^{131} .

updated as

$$\sigma_m^{2'} = \left(\sum_{k=1}^K p_{mk}^{old} \|x'_m - y_k\|^2 \right) / \sum_{k=1}^K p_{mk}^{old}. \quad (9)$$

Notice that the step size for slicing I_1 into patches should be small so that a certain pixel can be updated in different GMM models due to overlapped patches. The final output value of a certain pixel $I_{u,v}$ is calculated by simply averaging all the updated values located at (u, v) ,

$$I(u, v) = \frac{\sum_{i,m} \mathbb{1}(pos_m^i = (u, v)) x_m^i}{\sum_{i,m} \mathbb{1}(pos_m^i = (u, v))}, \quad (10)$$

where pos_m^i denotes the position of pixel m in the i -th patch, x_m^i denotes the pixel intensity of m in the i -th patch. $\mathbb{1}$ is an indicator function. See Fig. 4 for an example.

F. Optical Flow Update

Blur hinders accurate estimation of optical flow, which can possibly lead to inaccurate matches in finding patch correspondences. To mitigate this issue, we alternate optical flow and the EM algorithm for multiple iterations. I_1^t denotes the deblurred result in the t -th iteration (T times in total), and is used to compute the optical flow in the $(t+1)$ -th iteration. Updating optical flow increases the confidence of the patch correspondences.

G. Detail Layer

We extract the sharp features from I_2 and add it back to I_1^T to further preserve the details. A similar idea has been used in [58]. Since the noise in I_2 can negatively affect the quality of the detail layer, we apply the bilateral filter [48] to I_2 at first.

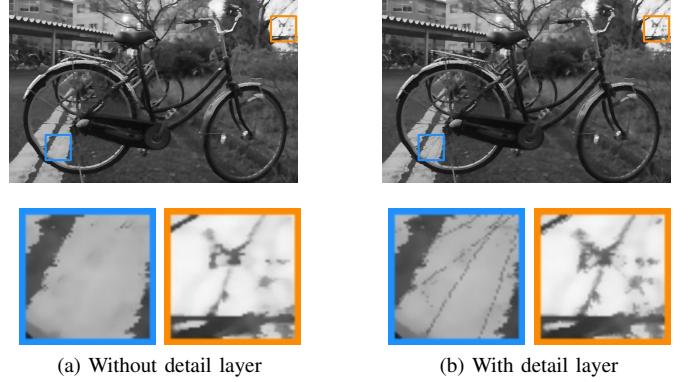


Fig. 5: Deblurred results with and without adding the detail layer: (a) without adding the detail layer, (b) with adding the detail layer.

Algorithm 1 Adding detail layer (DL)

Input: Deblurred image I_1^T , enhanced noisy image I_2 , constant threshold $\tau \in [10, 150]$, detail weight $\eta \in [0.1, 0.5]$

Output: Deblurred image with sharp features added

- 1: Apply bilateral filter to I_2
 - 2: Apply Laplacian filter to I_2 to obtain mask image I_m
 - 3: **for** every pixel located at (u, v) in I_1^T **do**
 - 4: Find the correspondence according to vector in DOF field from (u, v) in I_1^T to (u', v') in I_2
 - 5: **if** $I_m(u', v') > \tau$ **then**
 - 6: $I_1^T(u, v) \leftarrow (1 - \eta)I_1^T(u, v) + \eta I_2(u', v')$
 - 7: **end if**
 - 8: **end for**
 - 9: **return** Updated I_1^T
-

We then obtain a mask I_m by applying the Laplacian filter [8] to I_2 , to select the retained details. Since the I_2 and I_1^T are in different views, we use the DOF filed between them to find the spatial correspondence (see Sec. III-A). We can observe from Fig. 5 that the details are better recovered by adding the detail layer. The algorithm of adding details is listed in Alg. 1. The proposed deblurring algorithm is summarized in Alg. 2.

H. Key Parameters, Time Complexity and Convergence

To gain insights into the impact of parameters on OGMM, we analyze the influence of the key parameters (i.e., patch size in I_1 : s_1 , patch size in I_2 : s_2 , noise weight: ω) on the deblurring results (Fig. 6). We also give a brief discussion on time complexity.

We first discuss the effect of patch size (Fig. 6(b)~(g)). s_1 and s_2 directly relate to M and K , respectively, as mentioned in Sec. III-A. s_2 is required to be larger than s_1 to ensure a sufficient number of pixels in the corresponding noisy patch for running OGMM. Specifically, an equal patch size ($s_1 = s_2$) or a larger s_1 may weaken the ability of our method to capture a decent intensity distribution. The low PSNR in Fig. 6(k) accounts for a less decent outcome for the equivalent patch size. It can be observed from Fig. 6(b)~(g) that the increase of

Algorithm 2 Image deblurring (OGMM+DL)

Input: Blurred image I_1 , enhanced noisy image I_2 , iteration times T , termination number γ

Output: Deblurred image I_1^T

- 1: Parameters setting: $\sigma_m^2 \in [100, 500]$, $\omega = 0.02$, $\lambda \in [0.75, 0.8]$
- 2: **for** $t = 1$ to T **do**
- 3: Update optical flow and find corresponding patches with respect to I_1^{t-1} and I_2 ($I_1^0 = I_1$)
- 4: **for** Each patch in I_1^{t-1} **do**
- 5: Initialize centroids by X
- 6: **repeat**
- 7: E-step: update each p_{mk}^{old} by Eq. (3)
- 8: M-step: update each x_m and σ_m^2 by Eq. (8) and Eq. (9)
- 9: **until** γ is reached
- 10: **end for**
- 11: Obtain I_1^t via Eq. (10)
- 12: **end for**
- 13: Add details to I_1^T by Alg. 1
- 14: **return** I_1^T

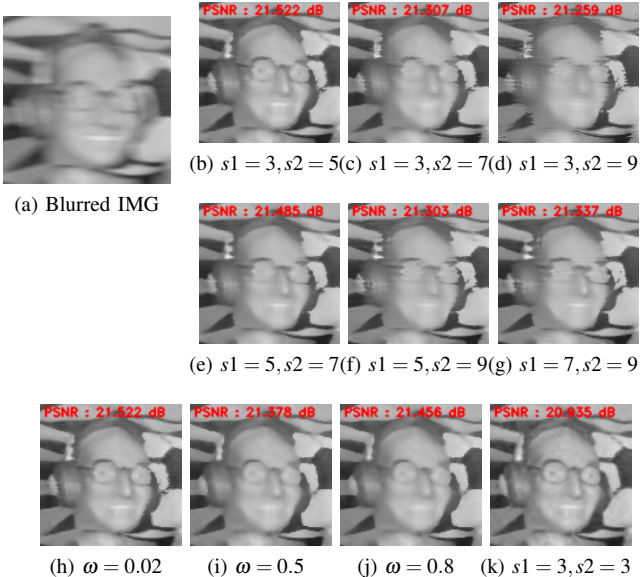


Fig. 6: Comparison of different parameter settings (s_2, s_1, ω) on the deblurring results of (a). (b)~(d), (e)~(g), and (h)~(j) explain the influence of s_2, s_1 and ω , respectively. (k) describes the deblurring result under equal patch size ($s_1 = s_2$).

s_1/M and s_2/K leads to worse deblurred results. This is mainly because the larger s_2/K is, the less relevant information in the noisy patch which corresponds to the blurred patch is involved. In addition, a larger s_1/M contains more blurred pixels. If the estimated optical flow is not sufficiently accurate, it will lead to unnatural results. Based on these observations, we empirically set $s_1 = 3, s_2 = 5$ as it achieves decent deblurring results in general. As for ω , which accounts for “outliers”, we empirically found that $\omega = 0.02$ is a good choice in terms of both deblurring and preserving details. A greater ω will

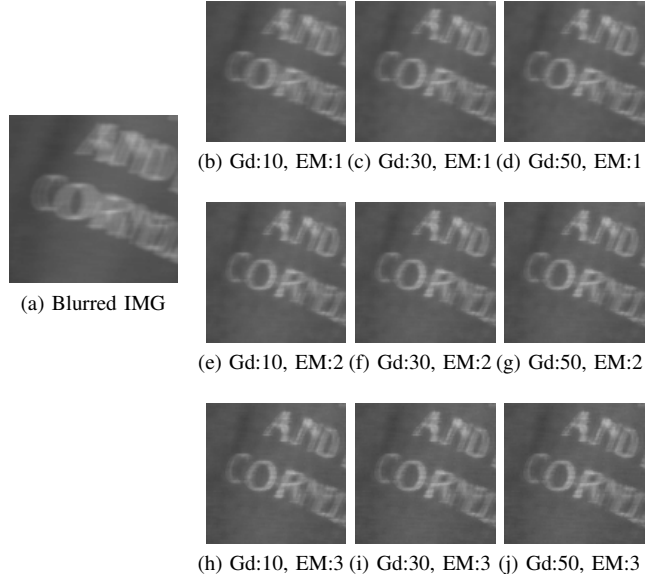


Fig. 7: An example of intermediate deblurred results produced at different gradient descent iterations in each round of EM update. Gd and EM denote the gradient descent iteration in one EM update, respectively.

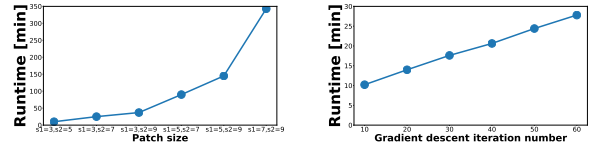


Fig. 8: The running time with respect to the patch size (left) and the number of iterations (right).

degrade the performance, as shown in Fig. 6(h)~(j).

Similar to other EM-based algorithms, such as [35], [53], the complexity of our algorithm under EM framework mainly depends on the termination criterion and the size of data (patch size). Fig. 8 shows the changes of runtime with respect to the patch size (Fig. 6(b)~(g)) and the number of iterations (Fig. 6(b)). We observe that the runtime has an exponential-like relationship with the patch size and it is linearly proportional to the number of iterations. In addition, the curves of Eq. (2) with respect to the number of EM iterations with different parameter settings are shown in Fig. 9. It can be seen from Fig. 9(a,b,c) that the energy of Eq. (2) declines drastically in the first few iterations, and tend to be steady (i.e., converged) with increasing iterations. In practice, we empirically set the EM iteration number to 1 to 5, depending on the size of the image. In each iteration, 50 rounds of gradient descent are called. Fig. 7 shows an example of intermediate deblurred results produced at different gradient descent iterations in each round of EM update. It can be seen that the first EM update contributes the most to removing the blur ((Fig. 7(b)~(d))), comparing to the following updates (Fig. 7(e)~(j)). Also, a greater ω would lead to a slower convergence (Fig. 9(e,f)).

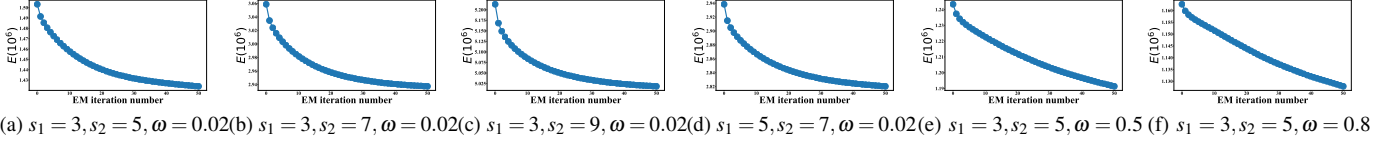


Fig. 9: Curves of Eq. 2 with respect to the EM iterations under different parameter settings.

TABLE I: Comparisons of average PSNR/SSIM/MSE on test images [4] which are corrupted with different types of synthetic blur. *BlurType1* is linear motion blur, *BlurType2* is circular motion blur, and *BlurType3* to *BlurType6* are complex blur mixed with multiple types of blur. See Fig. 10 for illustration.

	<i>BlurType1</i>	<i>BlurType2</i>	<i>BlurType3</i>
RL [40]	17.787 / 0.804 / 1244.060	18.766 / 0.822 / 1013.496	19.413 / 0.838 / 908.450
Deconvblind [24]	21.910 / 0.913 / 522.051	22.736 / 0.916 / 416.793	22.900 / 0.917 / 405.950
Whyte [52]	23.739 / 0.901 / 846.817	22.147 / 0.879 / 603.632	21.687 / 0.866 / 684.806
GFRS [27]	12.174 / 0.473 / 4305.645	13.531 / 0.550 / 3254.577	14.338 / 0.598 / 2758.658
GBBD [3]	23.823 / 0.921 / 496.064	23.128 / 0.906 / 409.134	22.687 / 0.902 / 451.751
Registration-1 [19], [7]	21.180 / 0.775 / 755.719	20.565 / 0.769 / 794.853	21.297 / 0.815 / 702.828
Registration-2 [1], [7]	21.667 / 0.860 / 578.877	20.178 / 0.825 / 813.343	20.257 / 0.817 / 802.075
SBD-single [64]	25.354 / 0.956 / 253.032	24.313 / 0.932 / 276.382	24.199 / 0.931 / 286.646
SBD-multi [64]	12.354 / 0.471 / 4356.241	12.728 / 0.499 / 3822.419	11.833 / 0.452 / 4521.26
GCRL+DL [58]	20.939 / 0.883 / 614.729	21.578 / 0.877 / 524.715	21.930 / 0.877 / 526.811
OGMM	27.905 / 0.966 / 144.208	25.046 / 0.944 / 230.982	25.295 / 0.947 / 225.836
OGMM+DL	27.716 / 0.966 / 141.942	25.133 / 0.945 / 226.747	25.410 / 0.948 / 220.014
	<i>BlurType4</i>	<i>BlurType5</i>	<i>BlurType6</i>
RL [40]	19.863 / 0.856 / 826.026	19.499 / 0.845 / 891.206	19.357 / 0.833 / 886.731
Deconvblind [24]	23.606 / 0.931 / 354.657	23.153 / 0.924 / 381.380	22.765 / 0.914 / 410.282
Whyte [52]	22.346 / 0.876 / 786.165	22.634 / 0.886 / 656.215	20.770 / 0.857 / 1011.524
GFRS [27]	14.145 / 0.594 / 2887.265	13.753 / 0.570 / 3168.338	14.526 / 0.598 / 2602.047
GBBD [3]	23.658 / 0.907 / 402.519	22.145 / 0.879 / 502.416	19.950 / 0.806 / 731.409
Registration-1 [19], [7]	21.917 / 0.822 / 659.675	21.926 / 0.823 / 662.619	21.033 / 0.812 / 728.168
Registration-2 [1], [7]	21.761 / 0.881 / 514.607	20.385 / 0.840 / 704.858	18.314 / 0.771 / 1122.865
SBD-single [64]	24.927 / 0.947 / 241.660	24.629 / 0.942 / 255.831	23.644 / 0.920 / 340.248
SBD-multi [64]	11.537 / 0.446 / 4748.240	11.938 / 0.470 / 4348.459	9.895 / 0.333 / 6891.413
GCRL+DL [58]	21.798 / 0.884 / 504.584	21.722 / 0.881 / 515.390	21.494 / 0.874 / 539.748
OGMM	26.277 / 0.958 / 188.181	25.937 / 0.954 / 203.715	24.724 / 0.940 / 257.072
OGMM+DL	26.453 / 0.959 / 180.985	26.087 / 0.955 / 196.959	24.811 / 0.942 / 252.102

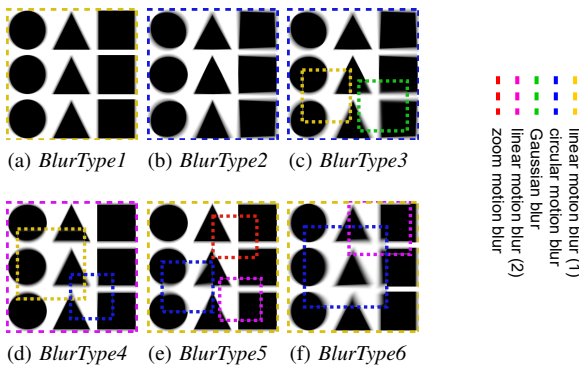


Fig. 10: Visualization of the six blur types in Tab. I. Dotted rectangles in different colors represent the regions corrupted with different types of blur. *BlurType3* to *BlurType6* are complex blur generated by fusing multiple types of blur.

IV. EXPERIMENTAL RESULTS

We evaluate our approach on both synthetic data and real-world data. Quantitative comparisons on synthetic data with ground truth are also carried out. Besides traditional methods [3], [24], [27], [40], [52], [58], [64], we also evaluate the performance of our model by comparing it with the state-

of-the-art deep learning based deblurring methods [29], [38]. Additionally, since our method depends on optical flow, we perform an analysis for it.

A. Synthetic Data

We first assess the performance of some current deblurring methods and our approach on ten image pairs from the publicly available dataset [4]. The dataset consists of multiple pairs of images taken from two different views in various scenes. To demonstrate the robustness of our method to different blur models, we synthetically generate six types of blur: (1) linear motion blur, (2) circular motion blur, (3) the mixture of circular motion blur, linear motion blur and Gaussian blur, (4) the mixture of two types of linear motion blur and circular motion blur, (5) the mixture of circular motion blur, zoom motion blur and two types of linear motion blur, and (6) the mixture of two types of linear motion blur and circular motion blur. The visualization of each type of blur is shown in Fig. 10. The first image in each pair is blurred with these six types of blur, respectively. Gaussian noise is added to the second image to generate the noisy image.

We compare our approach with the deblurring methods [58], [64] which can also take a pair of such images as input. *To our knowledge, deblurring using a pair of blurred/noisy images*

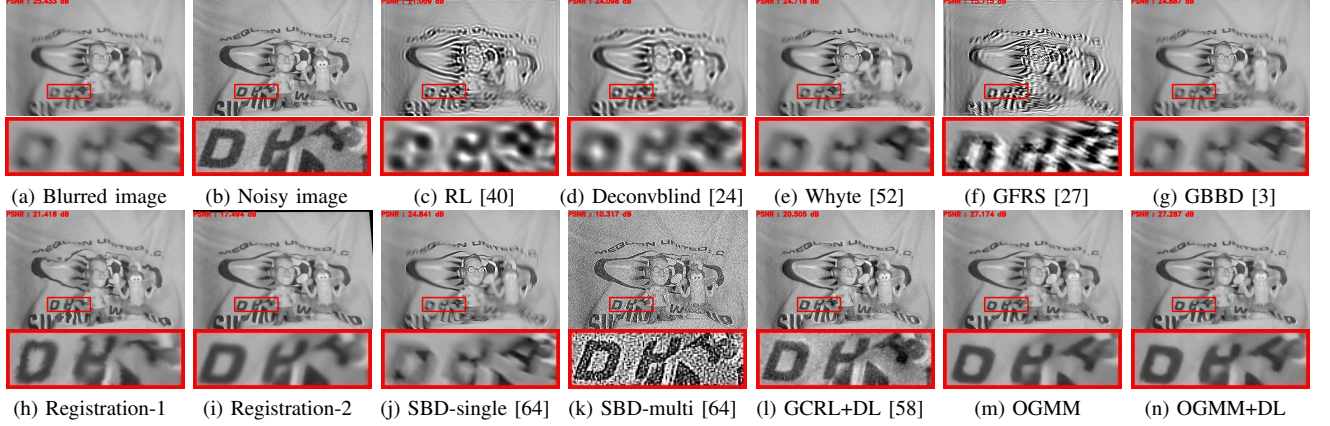


Fig. 11: Visual comparison on image *Mequon* in dataset [4] with synthetic blur (*BlurType3* in Fig. 10). (b) is added with Gaussian noise ($\sigma = 10$).

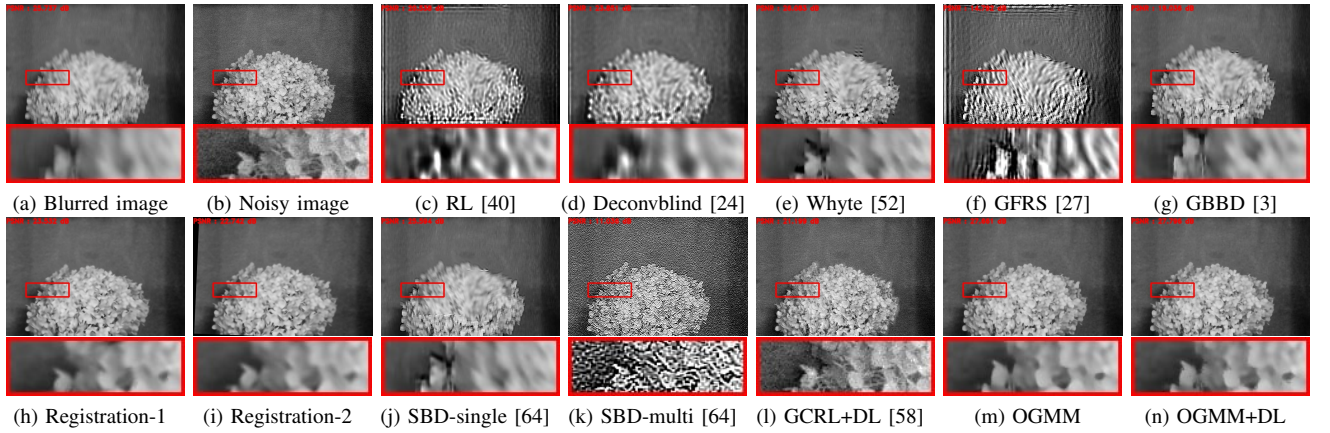


Fig. 12: Visual comparison on image *Hydrangea* in dataset [4] with synthetic blur (*BlurType4* in Fig. 10). (b) is added with Gaussian noise ($\sigma = 10$).

has been sparsely treated so far, and the method [58] is highly close to ours. We also compare our method with five single image deblurring methods [3], [27], [24], [40], [52], including two baseline methods [24], [40]. Note that the results of the single image blind deblurring methods are only reference results (produced with the available programs provided by authors), and they do not take advantage of the second image as input. In addition, we include the comparison against the pipeline of denoising and further alignment strategies [1], [7], [19] which can alternatively generate results from the view of the blurred image (see Sec. IV-B for more information).

As suggested by previous works [49], [50], we compute three metrics (in an average sense) for quantitative comparisons: peak signal-to-noise ratio (PSNR), structural similarity (SSIM) and mean square error (MSE). Tab. I displays the PSNR, SSIM and MSE, which are calculated between the deblurred images and the corresponding ground-truth image. We can see from Tab. I that our approach is more accurate than the two baseline methods [24], [40] and the state-of-the-art techniques [52], [58], [64], [3], [27]. Fig. 11 to Fig. 14 show the deblurring results under the mixup of different types of blur, by different deblurring methods. Notice that the close-up views focus on the blurred areas that are mixed by at least two kinds of blur.

We mainly discuss the results by [52], [58], [64], [3], [27] which are typically superior to [24], [40]. Fig. 11(h,i), Fig. 12(h,i), Fig. 13(h,i) and Fig. 14(h,i) respectively show two types of registration results (Registration-1 and Registration-2) between the blurred images (Fig. 11(a), Fig. 12(a), Fig. 13(a) and Fig. 14(a)) and the denoised versions of the noisy images (Fig. 11(b), Fig. 12(b), Fig. 13(b) and Fig. 14(b)) with [7], using dense optical flow (DOF) [19] and homography [1].

Single image [3], [27]. The method of [27] is a general kernel similarity-based non-blind single image deblurring approach which states that nonlinear motion blur can be addressed. Its deblurring results, presented in Fig. 11(f), Fig. 12(f), Fig. 13(f), and Fig. 14(f), contain a large amount of ringing artifacts, which is due to the difficulty in correctly estimating its kernel similarity matrix for highly complex blur kernels. A similar issue occurs in the method of [3], which is a blind deblurring approach designed to deal with uniform blur via a combined regularization using re-weighted graph TV priors. Obviously, the mixup of different types of blurs is beyond its capacity. Tab. I reports the involved metric evaluation.

Single/Multiple images [64]. The method [64] can handle both single image and multiple images, and the authors suggest

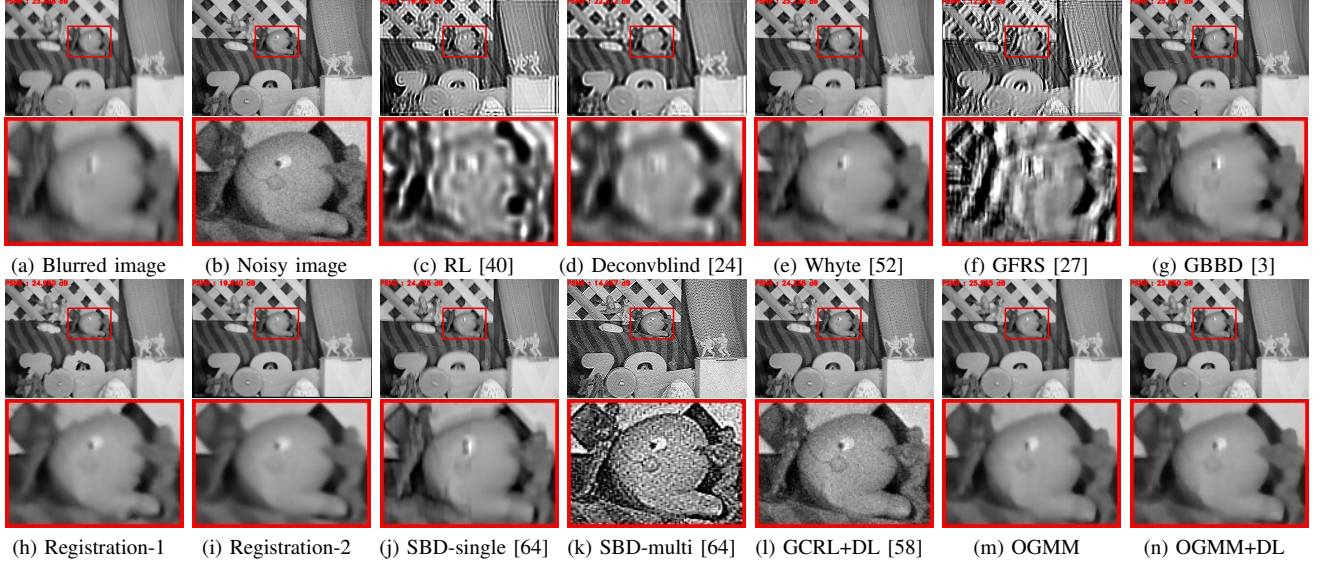


Fig. 13: Visual comparison on image *Army* in dataset [4] with synthetic blur (*BlurType5* in Fig. 10). (b) is added with Gaussian noise ($\sigma = 10$).

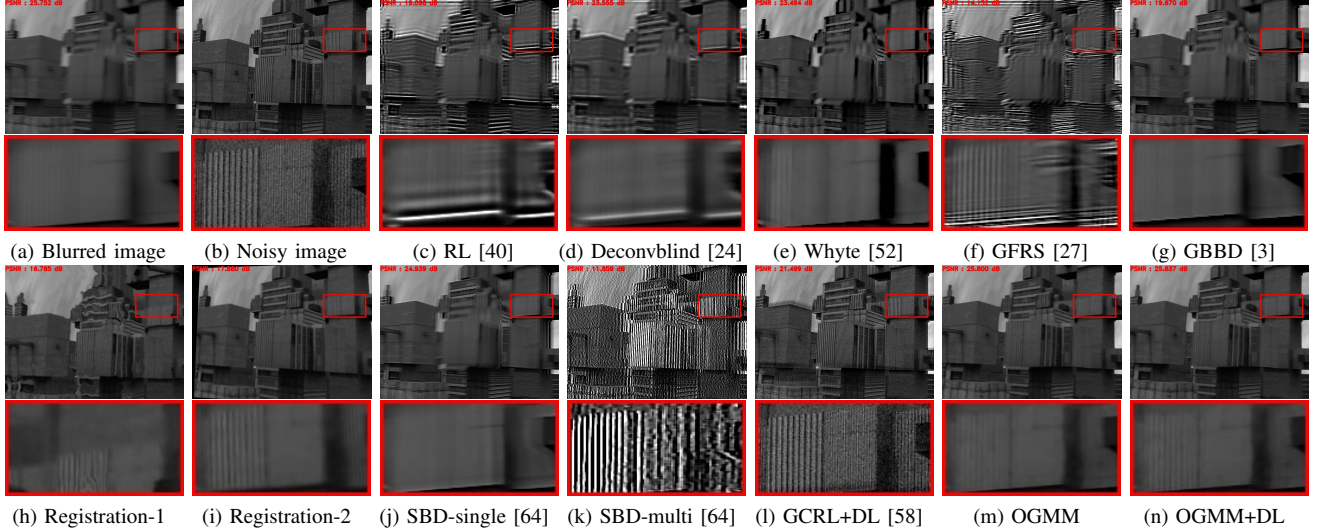


Fig. 14: Visual comparison on image *Urban* in dataset [4] with synthetic blur (*BlurType6* in Fig. 10). (b) is added with Gaussian noise ($\sigma = 10$).

that multiple input images can estimate the blur kernel more accurately. We thus show two versions of this method for comparison. Fig. 11(j), Fig. 12(j), Fig. 13(j), and Fig. 14(j) show the version of single image deblurring results of method [64]. Mixup of the space-variant and the space-invariant blur hinders the algorithm from estimating correct blur kernel, which is directly reflected by the blurry result and low PSNR values. This also accounts for that the single image deblurring version of [64] performs well on the linear motion blur case, but fails to deal with the remaining five types of non-uniform blur. For the version with multiple input images, despite the fact that the method [64] puts emphasis on automatically distinguishing blurred images from noisy images, it tends to mistake the noisy image for the blurred image and conduct deblurring to the noisy image (Fig. 11(k), Fig. 12(k), Fig. 13(k), and Fig. 14(k)).

This is because the proposed coupled penalty function in [64] judges that the intense blur leads to a higher degradation of the blurred image than the noisy image, thus unwillingly treating the noisy image as the dominant image.

Non-uniform blur [52]. The method of [52] stresses its advantage in handling non-uniform blur. Comparing to method [64], it produces clearer results and higher PSNR values. However, the mixup of blurs can cause obvious discontinuities, especially around the edges of dotted rectangles shown in Fig. 10, which increases the difficulty in estimating the blur kernel. For example, the close-up view in Fig. 13(e) shows the deblurring results close to the border of two different types of blurs. It is obvious that the border still clearly exists after deblurring by method [52], which confirms the limitation.

Blurred/noisy images pairs [58]. The method of [58]

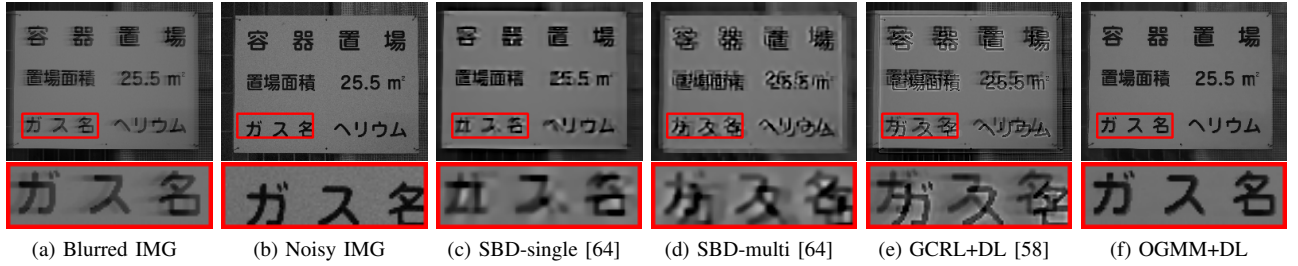


Fig. 15: Visual comparison on real-world data *Sign*. (a) Blurred image taken with the shutter speed of 0.5 second and ISO of 100. (b) Noisy image taken with the shutter speed of 0.01 second and ISO of 3200, and further enhanced by gamma correction ($\gamma = 1.5$). The close-up windows in (a) and (b) show different appearances because the two images are taken in different views.

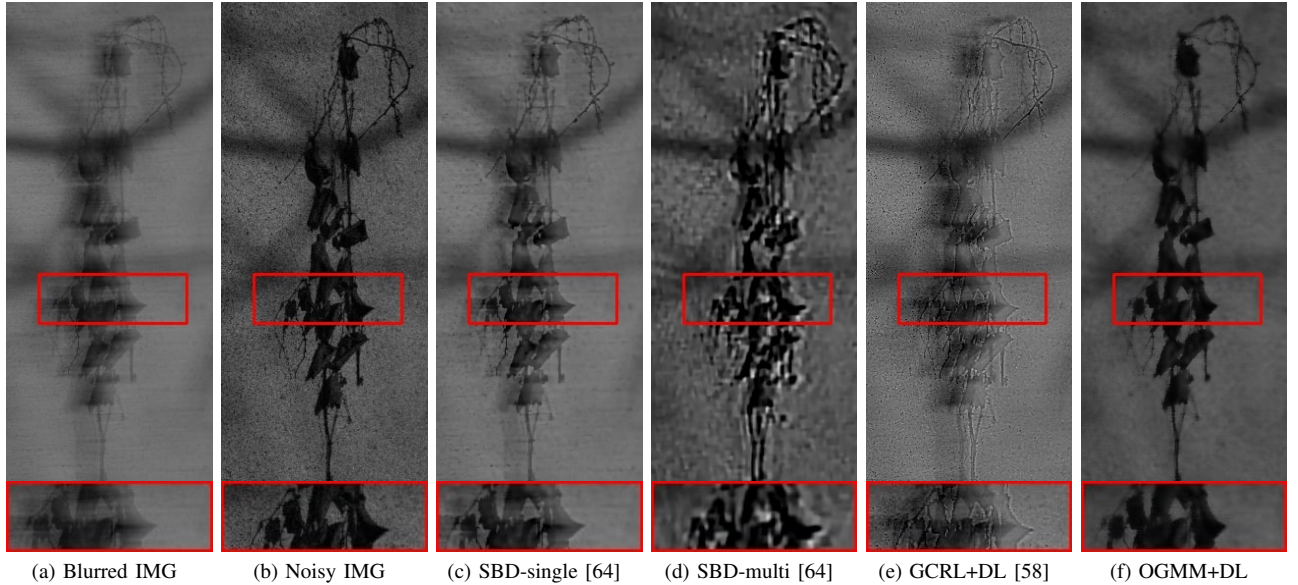


Fig. 16: Visual comparison on real-world data *licorice*. (a) Blurred image taken with the shutter speed of 0.5 second and ISO of 100. (b) Noisy image taken with the shutter speed of 0.005 second and ISO of 3200, and further enhanced by gamma correction ($\gamma = 2$). The close-up windows in (a) and (b) show different appearances because the two images are taken in different views.

utilizes paired blurred/noisy images for deblurring, requiring the same view for both images. As can be observed from Fig. 11(l), the result of [58] mixes both appearances of the blurred and the noisy images since the noisy image dominates the final result, which makes the deblurring result appears quite similar to the noisy image in Fig. 11(l). This may further result in “ghost area” when the difference of the capturing view angle gets larger (Fig. 15(l) and Fig. 16(l)). As a result, it has low PSNR and SSIM values, reflected in Tab. I.

Our method, in contrast, requiring no further adjustment or extra kernel modeling with respect to the blur types and the border-near areas, is able to generate more visually pleasing results with higher PSNR values, which shows robustness against complex blur. Also, it is worth pointing out that the final result can be further improved by adding a detail layer onto the output of OGMM, as shown in Fig. 11(n), Fig. 12(n), Fig. 13(n), and Fig. 14(n).

B. Real-World Data

We test our approach on various kinds of blurred/noisy image pairs which are captured in low light environments using an

off-the-shelf camera. Also, we compare our method with the state-of-the-art techniques [29], [58], [64].

We adopt the following procedure to take a real-world photo pair. First, we set a low ISO and a low shutter speed to obtain the blurred image. In the process of capturing, we add a camera shake, or move the object on purpose to produce stronger blur. Secondly, we use a high ISO and a high shutter speed to obtain the noisy image. Different from the synthetic data, the captured noisy images are too dark to use directly. Before deblurring, the noisy image is enhanced by synchronizing its brightness with the blurred image. The enhancement is achieved via gain/bias change and gamma correction, which also amplifies noise.

Fig. 15 to Fig. 17 exhibit visual comparisons on real-world data. The blur kernels estimated by [64], using single or multiple images, have difficulty in recovering the sharp image. The method [58] requires the same capturing view for the blurred/noisy image pair, which limits their applicability. As presented in the close-up view, it can be easily observed that heavy misalignment occurs when adding their generated detail layer back. The result by our method, without the need of kernel estimation, enjoys significantly better visual quality than

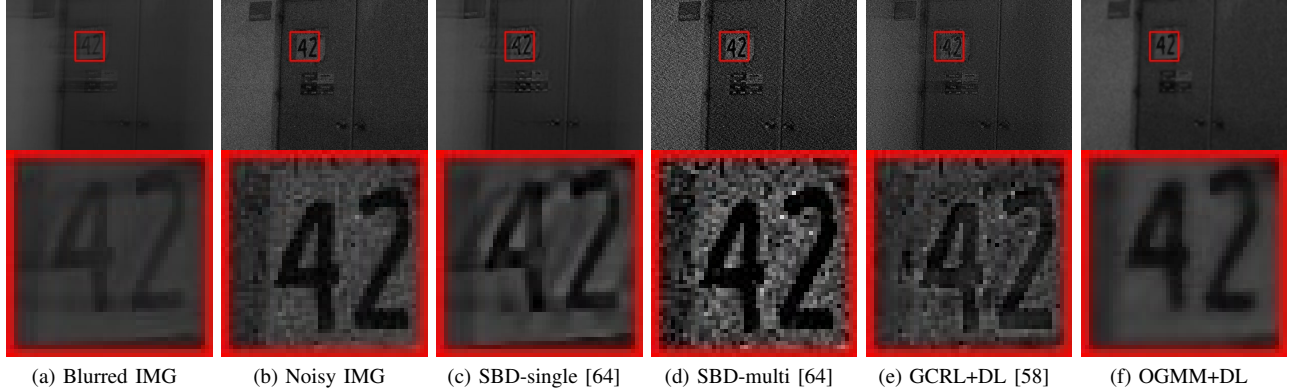


Fig. 17: Visual comparison on real-world data *Gate*. (a) Blurred image taken with the shutter speed of 2 second and ISO of 100. (b) Noisy image taken with the shutter speed of 0.01 second and ISO of 3200, and further enhanced by Gain correction ($\alpha = 2$) and Gamma correction ($\gamma = 2$). The close-up windows in (a) and (b) show different appearances because the two images are taken in different views.

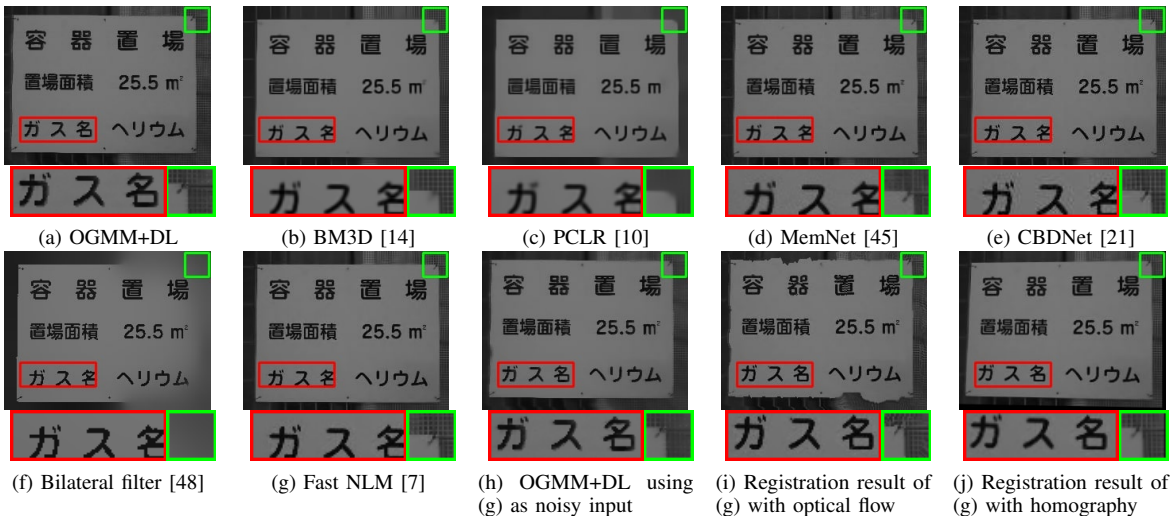


Fig. 18: (a) and (h) are the deblurring results of the blurred input (Fig. 15(a)) by OGMM without or with denoising the noisy input Fig. 15(b). (b)~(g) are the denoised results of Fig. 15(b). (i) and (j) are the results by aligning (g) with Fig. 15(a), by using two different correspondence estimation methods.

those by the state-of-the-art methods [58], [64]. Also, in the case of relatively large view difference, our method bridges two images from different view angles and can correctly correspond the patches in the blurred and noisy images. The deblurred result has the same view with the blurred input.

Discussion on alternative denoising and alignment.

Applying denoising and further alignment algorithms on the noisy image of the pair is an alternative for achieving a clear image corresponding to the blurred image. In Fig. 18 and Fig. 19, we show some visual results for some well-known denoising methods [7], [10], [14], [21], [45], [48], and registration/alignment techniques [19], [41]. As can be observed from Fig. 18(g) and Fig. 19(g), the method [7] induces “mosaics” around the character edges. In Fig. 18(b,c,f) and Fig. 19(b,c), methods [10], [14], [48] suffer from the same issue that the fine structures near the edges are smoothed out, which is one potential phenomenon of traditional denoising methods. The methods [21], [45] are two state-of-the-art deep

learning based denoising approaches. The method [45] builds dense connections among several types of memory blocks. The method [21] introduced a sub-network with asymmetric and total variation (TV) losses to specifically deal with real-world situations such as noise arising from in-camera processing. It can be clearly observed in Fig. 18(d) and Fig. 18(e) that they perform well on the areas with plain textures; however, noise around the context areas remains unresolved (please enlarge the corresponding areas for clear observations). In addition, both methods fail to handle intense real-world noise (Fig. 19(d,e)).

As shown in Fig. 18(h) (green box) and Fig. 19(h), in our method, denoising the noisy input inevitably leads to over-smoothness. Moreover, the view angle of the denoised image needs to be aligned with the blurred input. Fig. 18(i,j) and Fig. 19(i,j) are the results aligned by the correspondence provided by optical flow and homography [1], respectively. Obviously, these final “deblurred” results involve defects, such as distortion (Fig. 18(j) and Fig. 19(j)), misalignments (Fig. 18(i) and Fig.

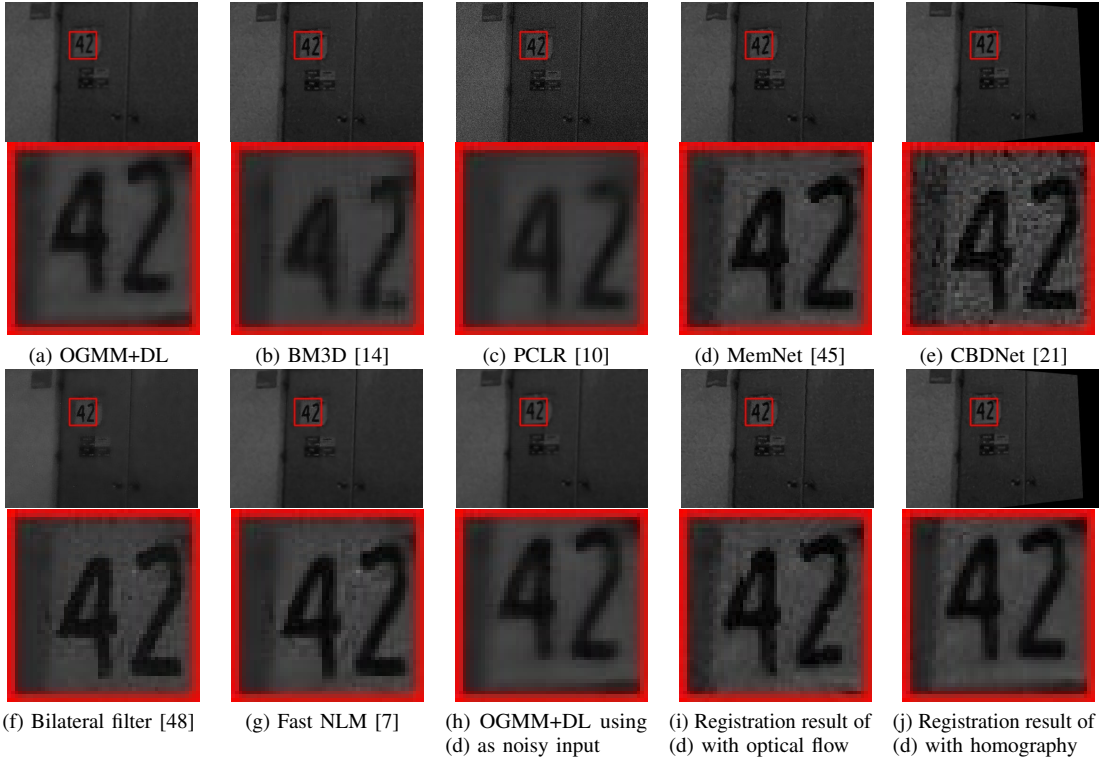


Fig. 19: (a) and (h) are the deblurring results of the blurred input (Fig. 17(a)) by OGMM without or with denoising the noisy input Fig. 17(b). (b)~(g) are the denoised results of Fig. 17(b). (i) and (j) are the results by aligning (d) with Fig. 17(a), by using two different correspondence estimation methods.

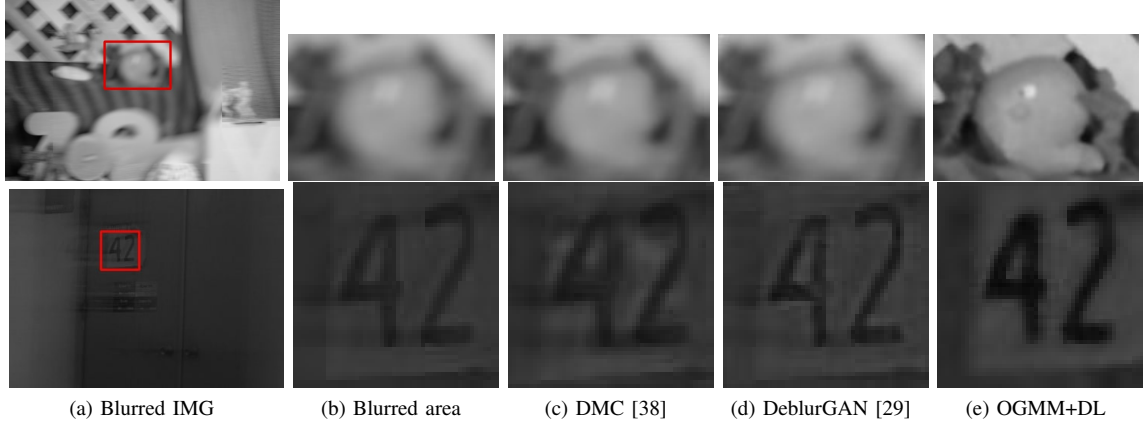


Fig. 20: Visual comparison with deep-learning based deblurring methods on both synthetic data *Army* (row 1) and real-world data *Gate* (row 2). Close-up views are shown for examining the details.

19(i)) and remaining noise (Fig. 19(i,j)). This is because the two input blurred and noisy images have limited quality and cannot provide sufficiently accurate correspondence estimation for alignment.

C. Comparison with Deep Learning based Methods

We also compare our approach with two major deep learning based deblurring methods [29], [38] which claimed their capability in dealing with complex blur with suggested parameters and trained models. We show the comparison results in Fig. 20.

Nah et al. developed an end-to-end, multi-scale CNN for recovering sharp images without blur kernel estimation [38]. Yet, its results in Fig. 20(c) seem to be less visually pleasant, since blur is only partially removed. The method of [29] resorts to a conditional adversarial network which is optimized using a multi-component loss function to free kernel estimation. As shown in Fig. 20(d), it can hardly remove the strong blur with a single blurred image as the input, in both cases of synthetic complex blur and real-world blur.

D. Analysis on Guiding Optical Flow

This subsection reports qualitative and quantitative analysis

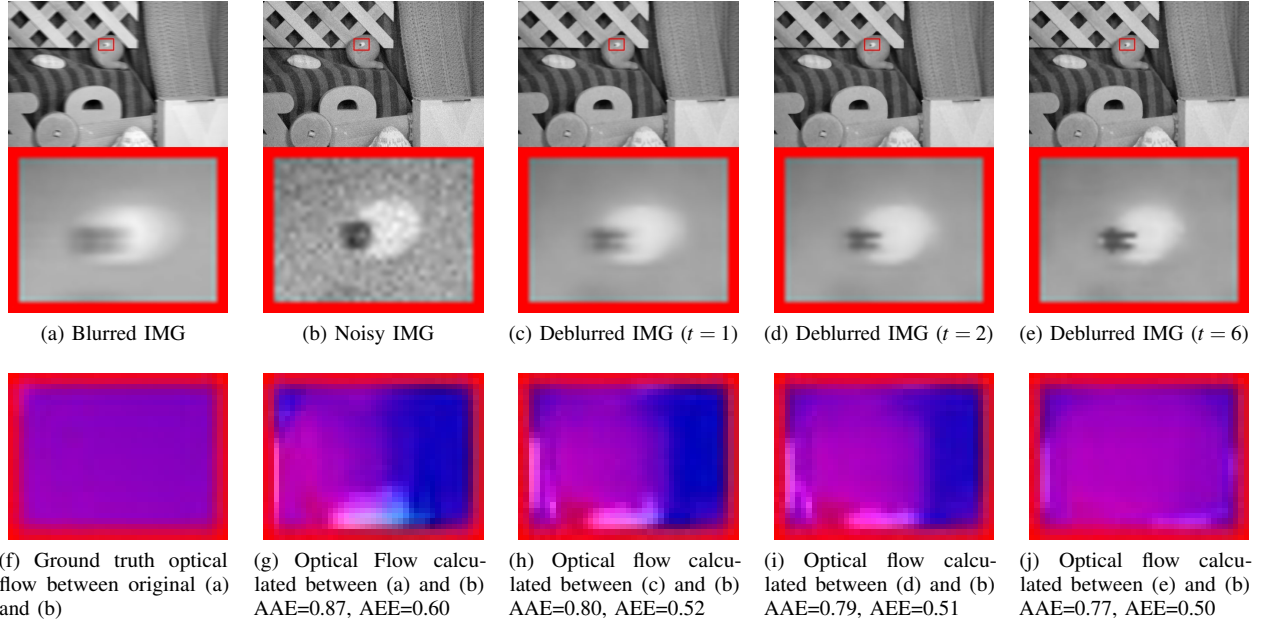


Fig. 21: Qualitative and quantitative analysis of the optical flow on image *RubberWhale* from dataset [4]. (a) is with the synthetic blur *BlurType1* in Fig. 10. (c)~(d) are deblurring results with respect to different numbers of iterations. (f)~(j) show the visualization of optical flow of the ROI area between the deblurring result and the noisy image using the color flow [4]. The update of the optical flow is introduced in Sec. III-F. Also, both the average absolute flow endpoint error (AAE) in pixel and the average angular error (AEE) in radian are shown with respect to the ground-truth flow.

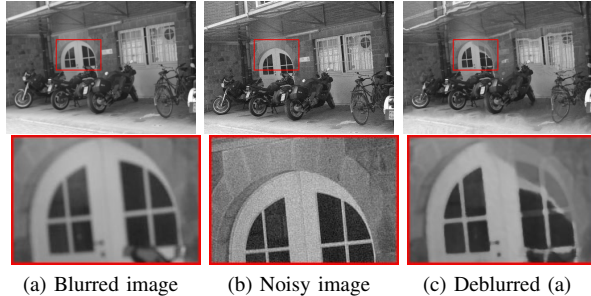


Fig. 22: A failure example. A large view difference deteriorates the accuracy of optical flow, thus leading to a distorted result.

on guiding optical flow. In our implementation, we simply adopt Farneback's original dense optical flow [19], which performs well due to small change of viewing angle between the input image pair.

Optical flow between the deblurred result and the noisy image is supposed to be refined iteratively. Fig. 21 shows an example of the update of optical flow along with the deblurring in Fig. 2. In Fig. 21(f), the ground-truth flow between the original Fig. 21(a) without blur and Fig. 21(b) without noise is taken as an evaluation basis. Fig. 21(g)~(j) show the optical flow calculated between the noisy image and the deblurred result with respect to different iteration times. As can be observed, with the increase of iteration times, the EM optimization iteratively removes the blur, and the optical flow shows clear improvement. Moreover, we show quantitative results in terms of the average absolute flow endpoint error

(AEE) [39] and the average angular error (AAE) [5], with respect to the ground-truth flow. Both the errors decrease along with the increase of the iteration numbers. It demonstrates that optical flow acts as a positive role in deblurring, and in return the deblurred image can also improve optical flow.

V. CONCLUSION

We proposed a novel, robust image deblurring method with the use of a pair of blurred/noisy images. Our approach first builds patch correspondences between the blurred and noisy images, and then relates the latent pixel intensities with the noisy pixel intensities under the GMM framework. We introduced a bilateral term for better features preservation. To refine the deblurred result, we extract and add a detail layer to it. Our approach is free of blur kernel estimation and robust to various types of blur. Extensive experiments over the synthetic and real-world data demonstrate that our method outperforms state-of-the-art techniques, in terms of both visual quality and quantity.

The major limitation of our method is its dependency on optical flow. If the motion gap between the two images is too large, the accuracy of optical flow deteriorates. As a result, this would alter object appearance or reshape some sharp features, as illustrated in Fig. 22. In the future, we would like to exploit more useful and effective relationship among patches to address the issue of undesired optical flow.

REFERENCES

- [1] E. Artin. *Geometric algebra*. Courier Dover Publications, 2016.

- [2] M. Arun and A. Rajagopalan. Hand-held low-light photography with exposure bracketing. In *2016 IEEE International Conference on Image Processing (ICIP)*, pages 1749–1753. IEEE, 2016.
- [3] Y. Bai, G. Cheung, X. Liu, and W. Gao. Graph-based blind image deblurring from a single photograph. *IEEE Transactions on Image Processing (TIP)*, 28(3):1404–1418, 2018.
- [4] S. Baker, D. Scharstein, J. Lewis, S. Roth, M. J. Black, and R. Szeliski. A database and evaluation methodology for optical flow. *International journal of computer vision (IJCV)*, 92(1):1–31, 2011.
- [5] J. L. Barron, D. J. Fleet, and S. S. Beauchemin. Performance of optical flow techniques. *International journal of computer vision (IJCV)*, 12(1):43–77, 1994.
- [6] C. M. Bishop et al. *Neural networks for pattern recognition*. Oxford university press, 1995.
- [7] A. Buades, B. Coll, and J.-M. Morel. A non-local algorithm for image denoising. In *Proceedings of the IEEE Conference on Computer Vision and Pattern Recognition (CVPR)*, volume 2, pages 60–65. IEEE, 2005.
- [8] P. Burt and E. Adelson. The laplacian pyramid as a compact image code. *IEEE Transactions on communications (TIP)*, 31(4):532–540, 1983.
- [9] J.-F. Cai, H. Ji, C. Liu, and Z. Shen. Blind motion deblurring using multiple images. *Journal of computational physics*, 228(14):5057–5071, 2009.
- [10] F. Chen, L. Zhang, and H. Yu. External patch prior guided internal clustering for image denoising. In *Proceedings of the IEEE international conference on computer vision (CVPR)*, pages 603–611. IEEE, 2015.
- [11] J. Chen, L. Yuan, C.-K. Tang, and L. Quan. Robust dual motion deblurring. In *Proceedings of the IEEE Conference on Computer Vision and Pattern Recognition (CVPR)*, pages 1–8. IEEE, 2008.
- [12] S. Cho, H. Cho, Y.-W. Tai, and S. Lee. Registration based non-uniform motion deblurring. In *Computer Graphics Forum (CGF)*, volume 31, pages 2183–2192. Wiley Online Library, 2012.
- [13] S. Cho and S. Lee. Fast motion deblurring. *ACM Transactions on Graphics (TOG)*, 28(5):145, 2009.
- [14] K. Dabov, A. Foi, V. Katkovnik, and K. Egiazarian. Image restoration by sparse 3d transform-domain collaborative filtering. In *Image Processing: Algorithms and Systems VI*, volume 6812, page 681207. International Society for Optics and Photonics, 2008.
- [15] M. Delbracio and G. Sapiro. Burst deblurring: Removing camera shake through fourier burst accumulation. In *Proceedings of the IEEE Conference on Computer Vision and Pattern Recognition (CVPR)*, pages 2385–2393, 2015.
- [16] M. Delbracio and G. Sapiro. Removing camera shake via weighted fourier burst accumulation. *IEEE Transactions on Image Processing (TIP)*, 24(11):3293–3307, 2015.
- [17] A. P. Dempster, N. M. Laird, and D. B. Rubin. Maximum likelihood from incomplete data via the em algorithm. *Journal of the royal statistical society. Series B (methodological)*, pages 1–38, 1977.
- [18] W. Dong, L. Zhang, G. Shi, and X. Wu. Image deblurring and super-resolution by adaptive sparse domain selection and adaptive regularization. *IEEE Transactions on image processing (TIP)*, 20(7):1838–1857, 2011.
- [19] G. Farnebäck. Two-frame motion estimation based on polynomial expansion. In *Scandinavian conference on Image analysis*, pages 363–370. Springer, 2003.
- [20] R. Fergus, B. Singh, A. Hertzmann, S. T. Roweis, and W. T. Freeman. Removing camera shake from a single photograph. *ACM Transactions on Graphics (TOG)*, 25(3):787–794, 2006.
- [21] S. Guo, Z. Yan, K. Zhang, W. Zuo, and L. Zhang. Toward convolutional blind denoising of real photographs. In *Proceedings of the IEEE Conference on Computer Vision and Pattern Recognition (CVPR)*, pages 1712–1722, 2019.
- [22] S. Hee Park and M. Levoy. Gyro-based multi-image deconvolution for removing handshake blur. In *Proceedings of the IEEE Conference on Computer Vision and Pattern Recognition (CVPR)*, pages 3366–3373. IEEE, 2014.
- [23] M. Hirsch, S. Sra, B. Schölkopf, and S. Harmeling. Efficient filter flow for space-variant multiframe blind deconvolution. In *Proceedings of the IEEE conference on Computer Vision and Pattern Recognition (CVPR)*, pages 607–614. IEEE, 2010.
- [24] T. J. Holmes, S. Bhattacharyya, J. A. Cooper, D. Hanzel, V. Krishnamurthi, W.-c. Lin, B. Roysam, D. H. Szwarczki, and J. N. Turner. Light microscopic images reconstructed by maximum likelihood deconvolution. In *Handbook of biological confocal microscopy*, pages 389–402. Springer, 1995.
- [25] Z. Hu, S. Cho, J. Wang, and M.-H. Yang. Deblurring low-light images with light streaks. In *Proceedings of the IEEE Conference on Computer Vision and Pattern Recognition (CVPR)*, pages 3382–3389. IEEE, 2014.
- [26] N. Joshi, R. Szeliski, and D. J. Kriegman. Psf estimation using sharp edge prediction. In *Proceedings of the IEEE Conference on Computer Vision and Pattern Recognition (CVPR)*, pages 1–8. IEEE, 2008.
- [27] A. Kheradmand and P. Milanfar. A general framework for regularized, similarity-based image restoration. *IEEE Transactions on Image Processing (TIP)*, 23(12):5136–5151, 2014.
- [28] D. Krishnan, T. Tay, and R. Fergus. Blind deconvolution using a normalized sparsity measure. In *Proceedings of the IEEE Conference on Computer Vision and Pattern Recognition (CVPR)*, pages 233–240. IEEE, 2011.
- [29] O. Kupyn, V. Budzan, M. Mykhailych, D. Mishkin, and J. Matas. Deblurgan: Blind motion deblurring using conditional adversarial networks. In *Proceedings of the IEEE conference on computer vision and pattern recognition (ICPR)*, pages 8183–8192, 2018.
- [30] A. Levin, Y. Weiss, F. Durand, and W. T. Freeman. Understanding and evaluating blind deconvolution algorithms. In *Proceedings of the IEEE Conference on Computer Vision and Pattern Recognition (CVPR)*, pages 1964–1971. IEEE, 2009.
- [31] W. Li, J. Zhang, and Q. Dai. Exploring aligned complementary image pair for blind motion deblurring. In *Proceedings of the IEEE Conference on Computer Vision and Pattern Recognition (CVPR)*, pages 273–280. IEEE, 2011.
- [32] X. Lu, H. Chen, S.-K. Yeung, Z. Deng, and W. Chen. Unsupervised articulated skeleton extraction from point set sequences captured by a single depth camera. pages 7226–7234, 2018.
- [33] X. Lu, Z. Deng, J. Luo, W. Chen, S.-K. Yeung, and Y. He. 3d articulated skeleton extraction using a single consumer-grade depth camera. *Computer Vision and Image Understanding*, 188:102792, 2019.
- [34] X. Lu, S. Wu, H. Chen, S. Yeung, W. Chen, and M. Zwicker. Gpf: Gmm-inspired feature-preserving point set filtering. *IEEE Transactions on Visualization and Computer Graphics (TVCG)*, 24(8):2315–2326, Aug 2018.
- [35] E. Luo, S. H. Chan, and T. Q. Nguyen. Adaptive image denoising by mixture adaptation. *IEEE transactions on image processing*, 25(10):4489–4503, 2016.
- [36] A. Mahalakshmi and B. Shanthini. A survey on image deblurring. In *Proceedings of the International Conference on Computer Communication and Informatics (ICCCI)*, pages 1–5, Jan 2016.
- [37] A. Myronenko and X. Song. Point set registration: Coherent point drift. *IEEE transactions on pattern analysis and machine intelligence (TPAMI)*, 32(12):2262–2275, 2010.
- [38] S. Nah, T. Hyun Kim, and K. Mu Lee. Deep multi-scale convolutional neural network for dynamic scene deblurring. In *Proceedings of the IEEE Conference on Computer Vision and Pattern Recognition (CVPR)*, pages 3883–3891, 2017.
- [39] M. Otte and H.-H. Nagel. Optical flow estimation: advances and comparisons. In *Proceedings of the European conference on computer vision (ECCV)*, pages 51–60, 1994.
- [40] W. H. Richardson. Bayesian-based iterative method of image restoration. *JOSA*, 62(1):55–59, 1972.
- [41] E. Rublee, V. Rabaud, K. Konolige, and G. R. Bradski. Orb: An efficient alternative to sift or surf. In *Proceedings of the IEEE Conference on Computer Vision (ICCV)*, volume 11, page 2. Citeseer, 2011.
- [42] Q. Shan, J. Jia, and A. Agarwala. High-quality motion deblurring from a single image. *ACM Transactions on Graphics (TOG)*, 27(3):73, 2008.
- [43] F. Troubek and P. Milanfar. Robust multichannel blind deconvolution via fast alternating minimization. *IEEE Transactions on Image processing (TIP)*, 21(4):1687–1700, 2012.
- [44] L. Sun, S. Cho, J. Wang, and J. Hays. Good image priors for non-blind deconvolution. In *European Conference on Computer Vision (ECCV)*, pages 231–246. Springer, 2014.
- [45] Y. Tai, J. Yang, X. Liu, and C. Xu. Memnet: A persistent memory network for image restoration. In *Proceedings of the IEEE international conference on computer vision (ICCV)*, pages 4539–4547, 2017.
- [46] A. M. Teodoro, J. M. Bioucas-Dias, and M. A. Figueiredo. Image restoration and reconstruction using variable splitting and class-adapted image priors. In *Proceedings of the IEEE Conference on International Conference on Image Processing (ICCV)*, pages 3518–3522. IEEE, 2016.
- [47] A. M. Teodoro, J. M. Bioucas-Dias, and M. A. Figueiredo. Image restoration with locally selected class-adapted models. In *Machine Learning for Signal Processing (MLSP), 2016 IEEE 26th International Workshop on*, pages 1–6. IEEE, 2016.
- [48] C. Tomasi and R. Manduchi. Bilateral filtering for gray and color images. In *Computer Vision, 1998. Sixth International Conference on*, pages 839–846. IEEE, 1998.

- [49] F. Vankawala, A. Ganatra, and A. Patel. A survey on different image deblurring techniques. *International Journal of Computer Applications (IJCA)*, 116(13):15–18, 2015.
- [50] S. Vasu, V. Reddy Maligireddy, and A. Rajagopalan. Non-blind deblurring: Handling kernel uncertainty with cnns. In *Proceedings of the IEEE Conference on Computer Vision and Pattern Recognition (CVPR)*, pages 3272–3281. IEEE, 2018.
- [51] R. Wang and D. Tao. Recent progress in image deblurring. *arXiv preprint arXiv:1409.6838*, 2014.
- [52] O. Whyte, J. Sivic, A. Zisserman, and J. Ponce. Non-uniform deblurring for shaken images. *International journal of computer vision (IJCV)*, 98(2):168–186, 2012.
- [53] J. Xu, L. Zhang, W. Zuo, D. Zhang, and X. Feng. Patch group based nonlocal self-similarity prior learning for image denoising. In *Proceedings of the IEEE international conference on computer vision (ICCV)*, pages 244–252. IEEE, 2015.
- [54] L. Xu and J. Jia. Two-phase kernel estimation for robust motion deblurring. In *Proceedings of the European conference on computer vision (ECCV)*, pages 157–170. Springer, 2010.
- [55] L. Xu, S. Zheng, and J. Jia. Unnatural l0 sparse representation for natural image deblurring. In *Proceedings of the IEEE conference on computer vision and pattern recognition (CVPR)*, pages 1107–1114. IEEE, 2013.
- [56] X. Xu, J. Pan, Y.-J. Zhang, and M.-H. Yang. Motion blur kernel estimation via deep learning. *IEEE Transactions on Image Processing (TIP)*, 27(1):194–205, 2017.
- [57] Y. Yan, W. Ren, Y. Guo, R. Wang, and X. Cao. Image deblurring via extreme channels prior. In *Proceedings of the IEEE Conference on Computer Vision and Pattern Recognition (CVPR)*, pages 4003–4011. IEEE, 2017.
- [58] L. Yuan, J. Sun, L. Quan, and H.-Y. Shum. Image deblurring with blurred/noisy image pairs. *ACM Transactions on Graphics (TOG)*, 26(3):1, 2007.
- [59] Z. Zha, X. Yuan, B. Wen, J. Zhang, J. Zhou, and C. Zhu. Image restoration using joint patch-group-based sparse representation. *IEEE Transactions on Image Processing (TIP)*, 29:7735–7750, 2020.
- [60] Z. Zha, X. Yuan, B. Wen, J. Zhou, J. Zhang, and C. Zhu. A benchmark for sparse coding: When group sparsity meets rank minimization. *IEEE Transactions on Image Processing (TIP)*, 29:5094–5109, 2020.
- [61] Z. Zha, X. Yuan, J. Zhou, C. Zhu, and B. Wen. Image restoration via simultaneous nonlocal self-similarity priors. *IEEE Transactions on Image Processing (TIP)*, 29:8561–8576, 2020.
- [62] Z. Zha, X. Zhang, Q. Wang, Y. Bai, and L. Tang. Image denoising using group sparsity residual and external nonlocal self-similarity prior. *arXiv preprint arXiv:1701.00723*, 2017.
- [63] H. Zhang and L. Carin. Multi-shot imaging: joint alignment, deblurring and resolution-enhancement. In *Proceedings of the IEEE Conference on Computer Vision and Pattern Recognition (CVPR)*, pages 2925–2932, 2014.
- [64] H. Zhang, D. Wipf, and Y. Zhang. Multi-image blind deblurring using a coupled adaptive sparse prior. In *Proceedings of the IEEE Conference on Computer Vision and Pattern Recognition (CVPR)*, pages 1051–1058. IEEE, 2013.
- [65] J. Zhang, D. Zhao, and W. Gao. Group-based sparse representation for image restoration. *IEEE Transactions on Image Processing (TIP)*, 23(8):3336–3351, 2014.
- [66] L. Zhang, A. Deshpande, and X. Chen. Denoising vs. deblurring: Hdr imaging techniques using moving cameras. 2010.
- [67] X. Zhu, F. Šroubek, and P. Milanfar. Deconvolving psfs for a better motion deblurring using multiple images. In *Proceedings of the European Conference on Computer Vision (ECCV)*, pages 636–647. Springer, 2012.
- [68] S. Zhuo, D. Guo, and T. Sim. Robust flash deblurring. In *Proceedings of the IEEE Conference on Computer Vision and Pattern (CVPR)*, pages 2440–2447. IEEE, 2010.
- [69] D. Zoran and Y. Weiss. From learning models of natural image patches to whole image restoration. In *Proceedings of the IEEE Conference on Computer Vision (ICCV)*, pages 479–486. IEEE, 2011.
- [70] D. Zoran and Y. Weiss. Natural images, gaussian mixtures and dead leaves. In *Advances in Neural Information Processing Systems (NIPS)*, pages 1736–1744, 2012.



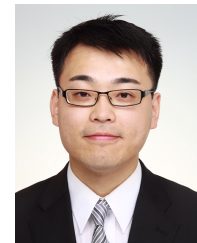
Chunzhi Gu Received his B.E. degree in June 2018 at University of Shanghai for Science and Technology (Shanghai, China), and is now pursuing Ph.D. degree at University of Fukui (Fukui, Japan) since April 2018. His current research focuses on modeling visual computing problems with probabilistic models, followed by optimization methods to estimate the parameters.



Xuequan Lu is a Lecturer (Assistant Professor) at Deakin University, Australia. He spent more than two years as a Research Fellow in Singapore. Prior to that, he earned his Ph.D at Zhejiang University (China) in June 2016. His research interests mainly fall into the category of visual computing, for example, geometry modeling, processing and analysis, animation/simulation, 2D data processing and analysis. More information can be found at <http://www.xuequanlu.com>.



Ying He is an associate professor at School of Computer Science and Engineering, Nanyang Technological University, Singapore. He received the BS and MS degrees in electrical engineering from Tsinghua University, China, and the PhD degree in computer science from Stony Brook University, USA. His research interests fall into the general areas of visual computing and he is particularly interested in the problems which require geometric analysis and computation. For more information, visit <http://www.ntu.edu.sg/home/yhe/>



Chao Zhang Received his Ph.D. degree at Iwate university (Japan) in March 2017. He is now a full-time assistant professor at department of engineering, university of Fukui (Japan) since April 2017. His research interests include computer vision , computer graphics, and evolutionary computing, mainly focused on applying optimization methods to solve visual computing problems.